

# Space weather-related to potentially destructive seismic activity recorded on a global scale

Gabriele Cataldi<sup>1</sup>, Valentino Straser<sup>2</sup>, Daniele Cataldi<sup>1,3</sup>

(1) Radio Emissions Project (I). ltpaobserverproject@gmail.com

(2) Department of Science and Environment UPKL Brussel (B). valentino.straser@gmail.com

(3) Fondazione Permanente G. Giuliani - Onlus (I). daniele77c@hotmail.it

## Abstract

This study discusses the potential relationship between the phenomena of solar origin and destructive seismic activity on a global scale. The seismic emergency requires the acquisition of new data in modern society to improve understanding of the triggering phenomena of earthquakes to activate preventive measures in defense of man and anthropogenic activities. Among the possible cause-effect relationships, potentially destructive earthquakes were compared with solar activity. In this research, 121 seismic zones of the world were analyzed and for each one particular characteristic was detected that goes beyond the mechanism of simple coincidence. Each seismic location turned out to be unique from the others, in response to geodynamics and crustal nature. The results are surprising and open new perspectives for the study of seismic precursors, but a contribution in the seismological, tectonic, and geophysical fields.

**Keywords:** earthquake prediction, proton density, electromagnetic seismic precursors, global seismicity, solar activity.

## Introduction

The global seismicity is a phenomenon that has been correlated to solar activity at the beginning of the twentieth century (G. Cataldi et al., 2019), but we can say that the most important discoveries on this type of correlation have only occurred in the last ten years (G. Cataldi, 2019; V. Straser et al., 2019). The analysis of solar activity and M6+ global seismic activity has allowed the authors to develop a seismic prediction method that is not based on the interpretation of historical data on seismicity but on the identification of precursor signals that have proved reliable over 9 years (from 1 January 2012 to 31 December 2019) and which currently allow the authors to establish, with an average advance of a few days, when a resumption of M6+ global seismic activity is expected. This result has already been achieved by analyzing the global M6+ seismicity and solar activity in 2012 (G. Cataldi et al., 2013): a year in which the authors were able to identify the precursor phenomenon of M6+ global seismic activity: the increases in the density of the solar ion flux (proton density). Unfortunately, the news did not get the right consideration and the hoped-for echo.

Through this work, the authors present the results of their study updated to 2019: results which once again confirm the observations made in previous years and the reliability of the seismic precursor that they have identified since 2012.

## Methods and data

The identification of a reliable seismic precursor capable of being related to the M6+ global seismic activity was not an easy task. The authors, in fact, carried out a large correlation study (started in 2012) through which they analyzed the characteristics and modulation of a series of electromagnetic phenomena that were related, with a certain frequency, to potentially destructive seismic events that occurred between 2009 and 2011:

- geomagnetic variations/perturbations recorded on angular and vector geomagnetic elements;
- variation of geomagnetic indices;
- solar wind parameters (velocity, density, temperature, dynamic pressure, etc.) concerning solar coronal mass ejection events (CMEs), sunspots, coronal hole, and solar flares;
- increase of the electromagnetic emissions on Earth's magnetic poles;
- reducing of the magnetopause standoff distance;
- Interplanetary Magnetic Field (IMF) variations/perturbations;

At the end of 2011, the authors realized that increases in solar ion flux (increases in the proton density of the solar wind) were the right candidates as they always preceded potentially destructive seismic events; so from January 1, 2012, the authors began to analyze the M6+ global seismic activity in relation to the increases in the proton density of the interplanetary medium and its characteristics. At the end of 2012, the data obtained confirmed that the increases in the proton density of the solar wind were closely related to the M6+ global seismic activity.

Coming to the present day, the authors measured the distribution of time intervals of the increases in solar ion flux (proton density) that preceded 1051 destructive seismic events (**Fig. 1**) recorded between 1 January 2012 and 31 December 2019 (corresponding to 100% of the M6+ seismic events that occurred on a global scale between 2012 and 2019, **Fig. 2**, **Fig. 3**) noting that 31.87% occurred during the initial phase of the ionic increase of the solar wind (A); 5.23% occurred during ( $\pm 6$  hours) the maximum recorded density level (B); 49.58% were recorded after the maximum density peak (C) and 13.32% of earthquakes were recorded during the final "normalization" phase of the density values (D). The energy fractions of the solar ion flux that the authors analyzed to carry out this study are: proton flux 761-1220 keV ( $\text{p}/(\text{cm}^2\text{-sec-ster-MeV})$ ); proton flux 1060-1900 keV ( $\text{p}/(\text{cm}^2\text{-sec-ster-MeV})$ ); proton flux 310-580 keV ( $\text{p}/(\text{cm}^2\text{-sec-ster-MeV})$ ); proton density  $\text{cm}^{-3}$ .

### Percentage of M6+ seismic events related to the ionic variation curve of interplanetary medium between 2012-2019

G. Cataldi, D. Cataldi, V. Straser

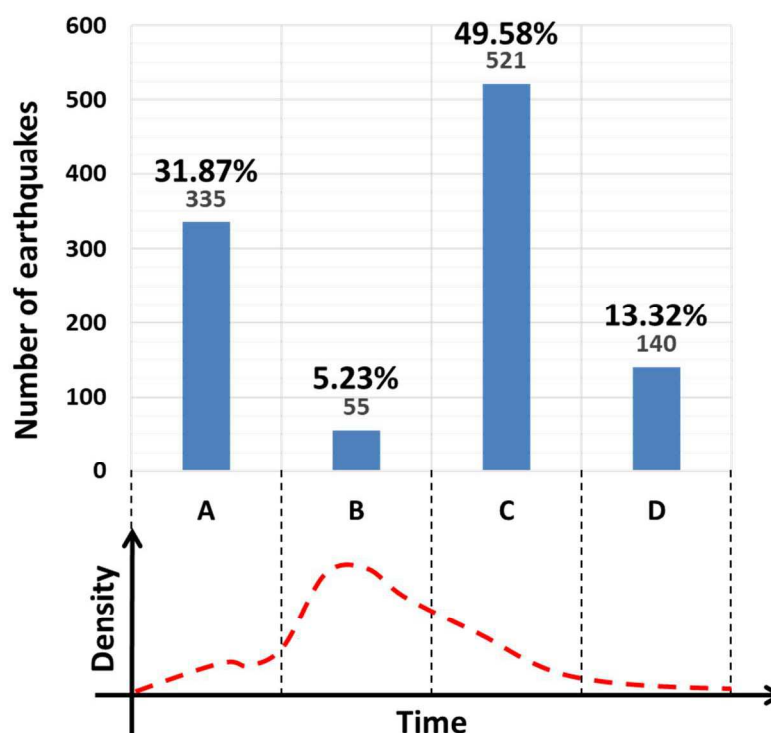


**Fig. 1 – Distribution of time intervals between the variation of the proton density of the solar wind and the seismic events related to it.** The graph above shows the distribution of the time intervals measured between the start of the proton increase of the solar wind recorded in the Lagrangian point L1 and the seismic events related to it. The graph was created by analyzing 1051 M6+ seismic events recorded between January 1, 2012 and December 31, 2019. The dashed red line represents the typical curve of a "gradual" proton increase that the authors have divided into four distinct phases: (A) initial phase of the increase; (B) maximum proton increase reached by the solar wind; (C) phase of reduction of the proton density; (D) phase of "normalization" of the proton density values. The numbers above the blue bars represent the number of seismic events that occurred during the phase of proton increase (A, B, C, D) indicated by the lower part of the graph. Credits: G. Cataldi, D. Cataldi, V. Straser, USGS, iSWA.

With the term "normalization" the authors mean the time in which, after a certain ionic increase in the solar wind, the density undergoes small oscillations tending to the definitive leveling which is equivalent to the basal

density level of the interplanetary medium, or to the minimum level density measured between two ion increments.

### Number of M6+ seismic events that occurred between 2012 and 2019

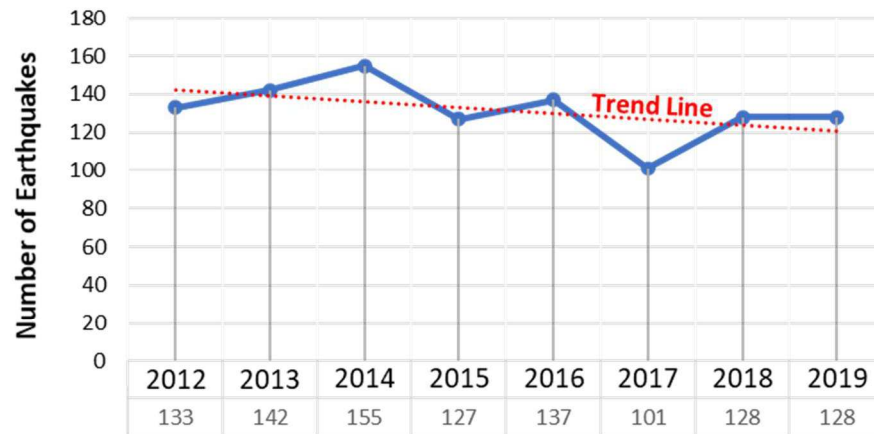


**Fig. 2 – Number of M6+ seismic events recorded on a global scale between 2012 and 2019.** The graph above shows the distribution of the number of potentially destructive seismic events (M6+) recorded between 1 January 2012 and 31 December 2019. The sample is equivalent to 1052 but the M6.2 earthquake that occurred in Tonga on 25 June 2017 was intentionally omitted in the statistical study as the data on the ionic variation of the solar wind provided by the Advanced Composition Explorer (ACE) Satellite located in Lagrangian orbit L1 were not available. Therefore the number of total M6+ seismic events was, for simplification, assimilated to 1051. The dashed red line represents the trend line of the number of destructive seismic events recorded between 2012 and 2019: it highlights a decrease in the number of seismic events confirming the progression of the “solar minimum” occurred in the final phase of the current solar cycle (SC24). Credits: G. Cataldi, D. Cataldi, V. Straser, USGS.

### Number of M6+ seismic events recorded monthly between 2012 and 2019

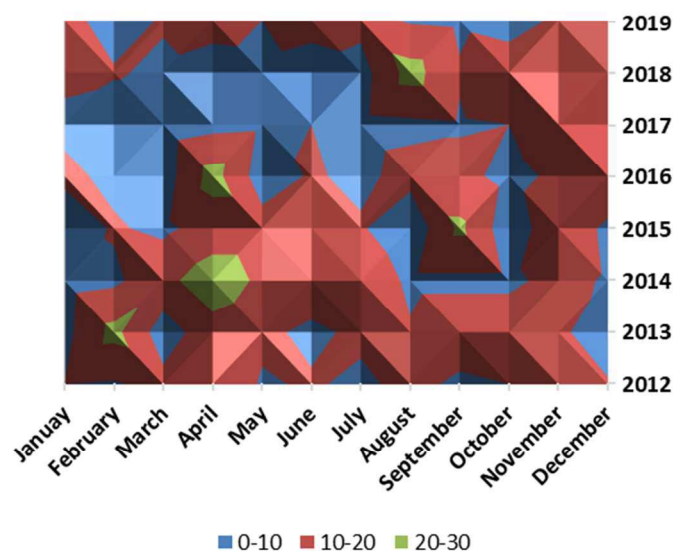


**Fig. 3 – Monthly distribution of M6+ seismic events number occurring on a global scale between 2012 and 2019.** The image above shows the monthly distribution of M6+ seismic events recorded on a global scale between 2012 and 2019: it is clear that the greatest number of seismic events was found in April 2014 and 2016; in August 2018, in September 2015 and in February 2013. Credits: G. Cataldi, D. Cataldi, V. Straser, USGS.

This type of study has shown that between 2012 and 2019 the “gradual” proton increases are those most correlated to a resumption of M6+ global seismic activity. In fact, only 6 M6+ seismic events (0.57%), out of a total of 1051, were preceded by an “impulsive” ionic increase, and only 4 seismic events (0.38%) out of 1051 total seismic events, were preceded by both the types of ion increments (**Fig. 4**).

### Gradual and impulsive increases compared

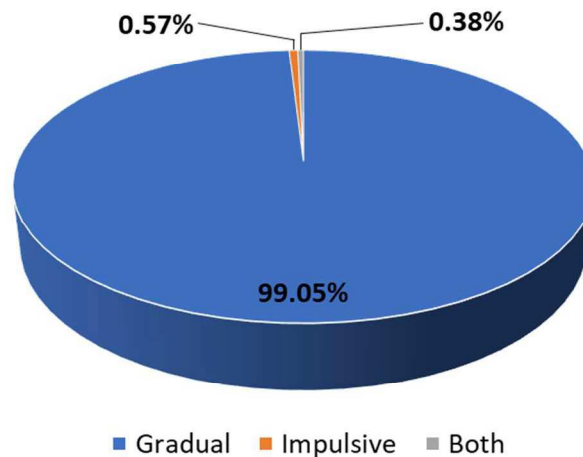


**Fig. 4 – Gradual and impulsive increases compared.** In the graph above, the distribution of M6+ seismic events occurred on a global scale was compared based on the type of ionic increase to which the seismic events were correlated. Credits: G. Cataldi, D. Cataldi, V. Straser.

“Gradual” ion increases are observed during solar coronal mass ejections (CMEs) or when the Earth intersects ion flows released from areas of the Sun's surface (e.g. sunspots) where electrically charged particles are trapped along with magnetic loops. The duration of a gradual ion increase is more than 24 hours and in some cases, it can last for a few weeks. Impulsive ion increases, on the other hand, generally last no more than 24 hours and are associated with solar flares (D. V. Reames, 2002).

The authors also analyzed the distribution of time intervals by calculating the average interval of each country in which a potentially destructive seismic event was recorded between 1 January 2012 and 15 July 2020. The following average intervals were obtained (**Fig. 5-11**):

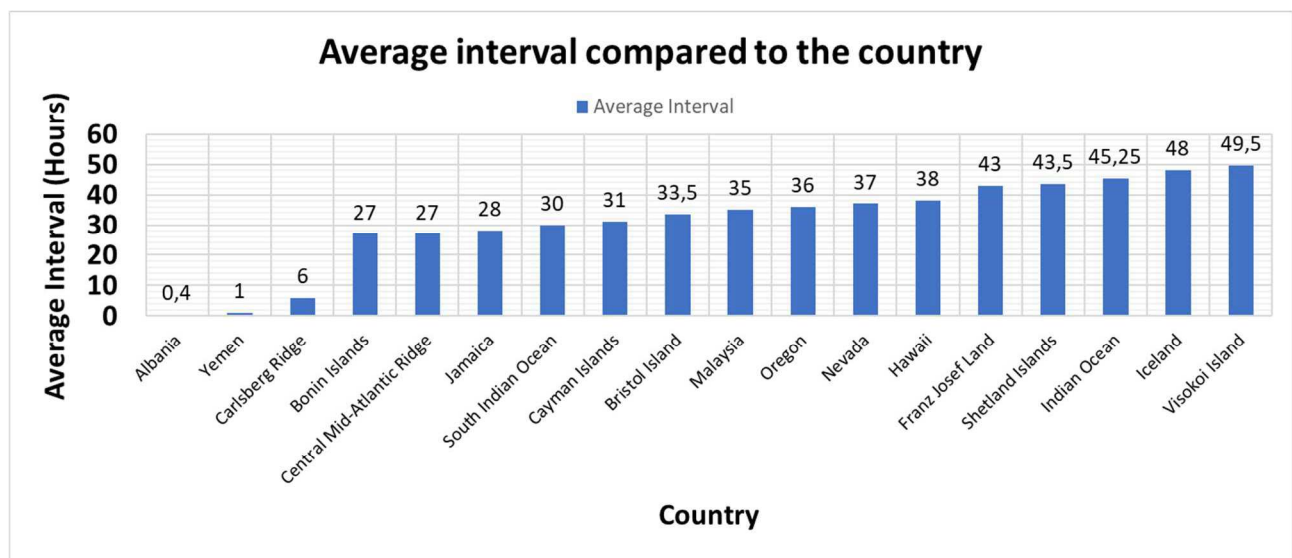


**Fig. 5 – Average interval compared to the country.** The image above shows the average intervals (expressed in hours) calculated for each single country in which the M6+ seismic events were recorded. Credits: G. Cataldi, D. Cataldi, V. Straser.



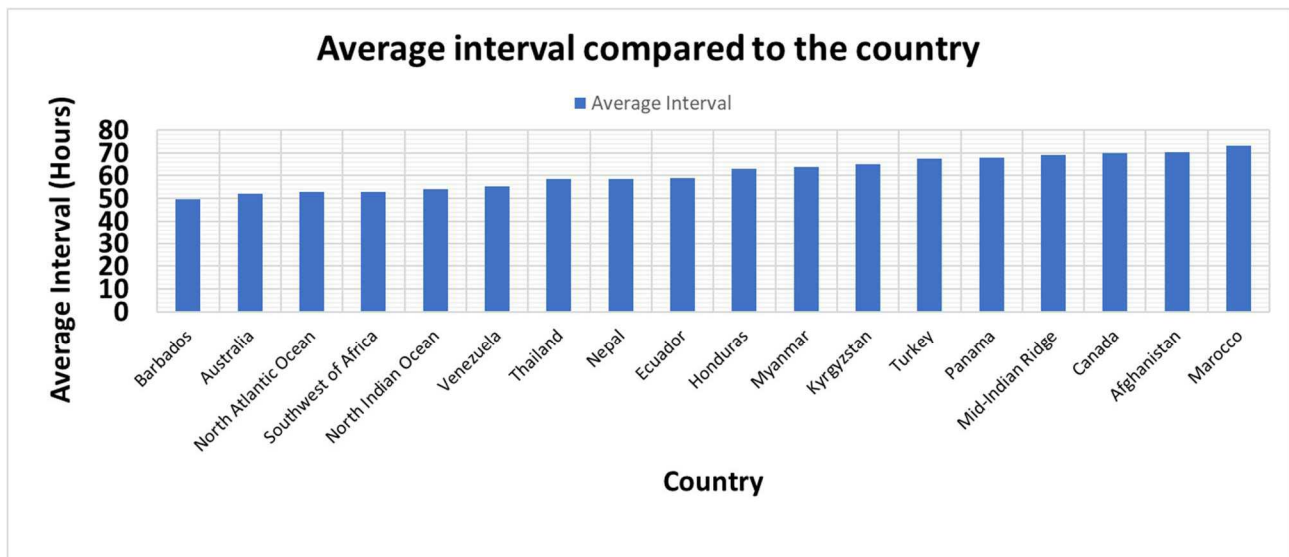


**Fig. 6 – Average interval compared to the country.** The image above shows the average intervals (expressed in hours) calculated for each single country in which the M6+ seismic events were recorded. Credits: G. Cataldi, D. Cataldi, V. Straser.

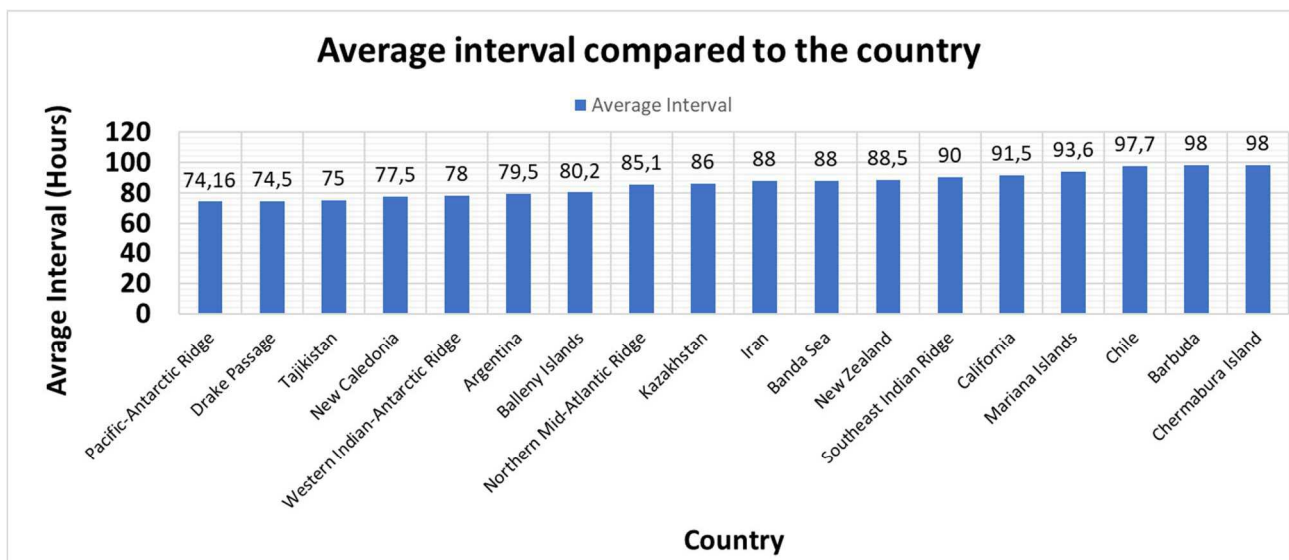


**Fig. 7 – Average interval compared to the country.** The image above shows the average intervals (expressed in hours) calculated for each single country in which the M6+ seismic events were recorded. Credits: G. Cataldi, D. Cataldi, V. Straser.

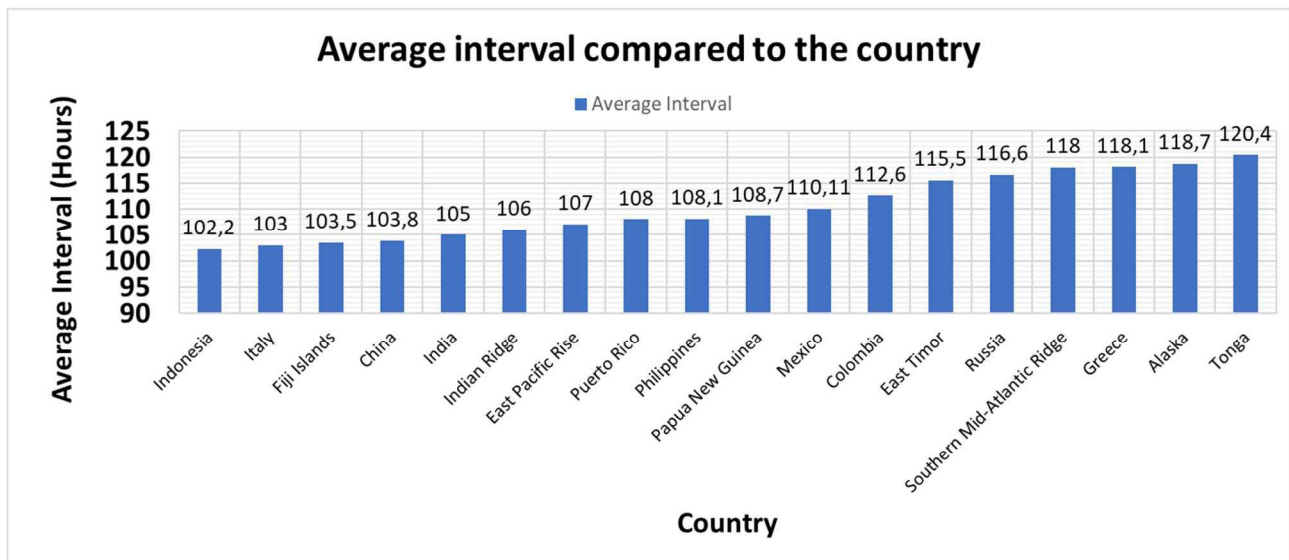


**Fig. 8 – Average interval compared to the country.** The image above shows the average intervals (expressed in hours) calculated for each single country in which the M6+ seismic events were recorded. Credits: G. Cataldi, D. Cataldi, V. Straser.

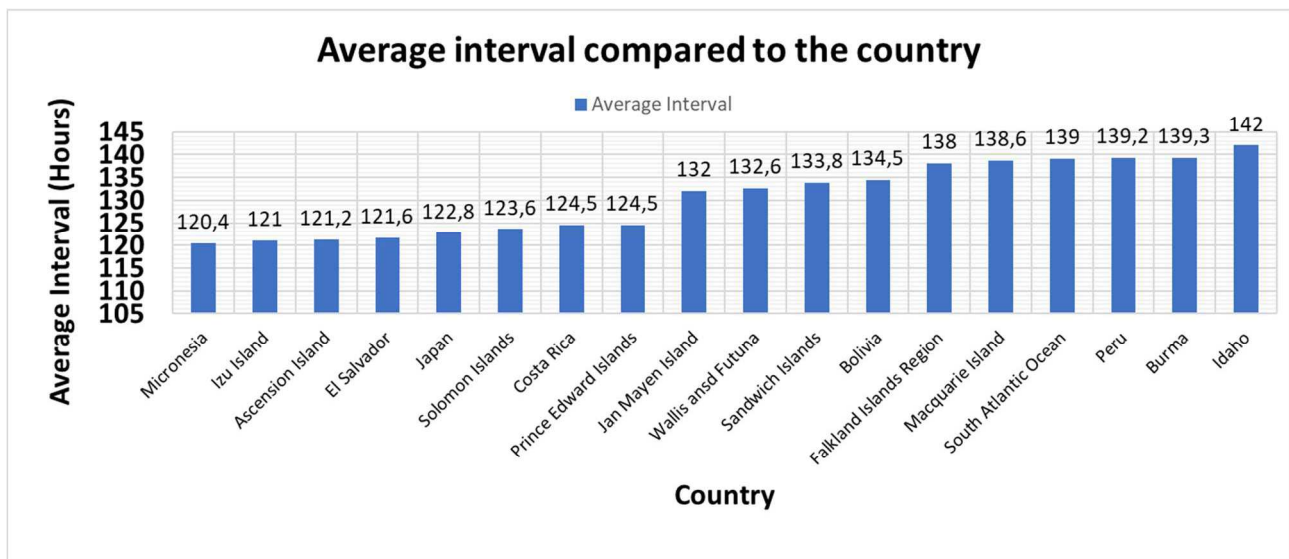


**Fig. 9 – Average interval compared to the country.** The image above shows the average intervals (expressed in hours) calculated for each single country in which the M6+ seismic events were recorded. Credits: G. Cataldi, D. Cataldi, V. Straser.

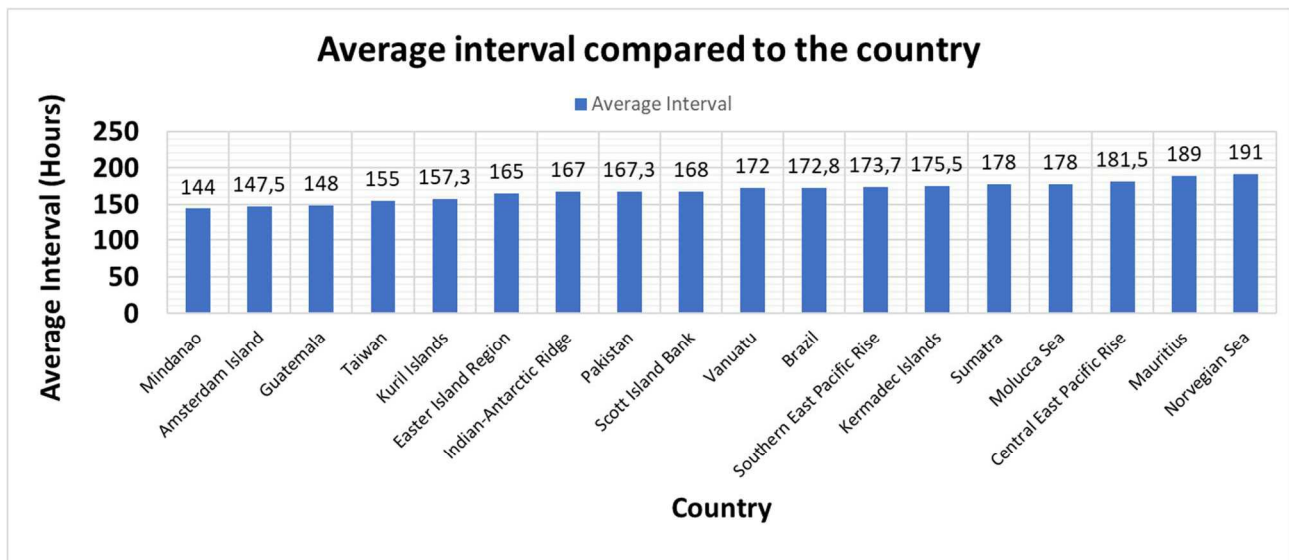


**Fig. 10 – Average interval compared to the country.** The image above shows the average intervals (expressed in hours) calculated for each single country in which the M6+ seismic events were recorded. Credits: G. Cataldi, D. Cataldi, V. Straser.

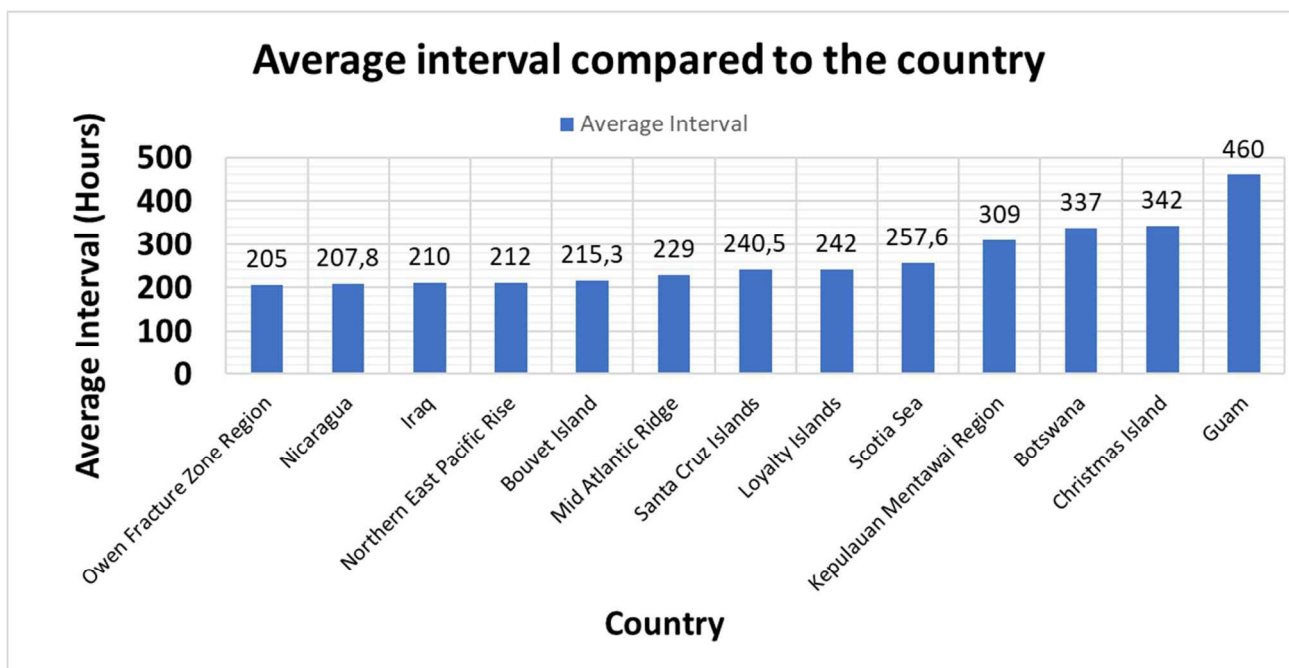


**Fig. 11 – Average interval compared to the country.** The image above shows the average intervals (expressed in hours) calculated for each single country in which the M6+ seismic events were recorded. Credits: G. Cataldi, D. Cataldi, V. Straser.

The average of the time intervals takes into account the number of seismic events that have been recorded in every single country. In the following areas or countries when only one seismic event was recorded, it was therefore not possible to calculate the average interval but the data indicated represents only the recorded time interval: Carlsberg Ridge, Australia, Albania, Jamaica, Cayman Islands, Idaho, Honduras, Nevada, Iceland, Franz Josef Land, Iraq, Southwest of Africa, Hawaii, Yemen, Chermabura Island, Botswana, Kyrgyzstan, Barbuda, Malaysia, Scott Island Bank, Owen Fracture Zone Region, Guam, Morocco, Southern Mid-Atlantic Ridge, Mid Atlantic Ridge, Central Mid-Atlantic Ridge, North Atlantic Ocean, Falkland Islands Region, South Atlantic Ocean, Mindanao, Myanmar, Kepulauan Mentawai Region, Norwegian Sea, Bonin Islands, Southeast Indian Ridge, North Indian Ocean, Indian-Antarctic Ridge, Indian Ridge, South Indian Ocean, Mid-Indian Ridge, Loyalty Islands.

The averages obtained range from 0.4 hours (the minimum average interval recorded), for Albania, to 460 hours (the maximum average interval recorded) for Guam. The standard deviation of average intervals (**Fig. 12**) showed that Shetland Islands had the lowest standard deviation (0.7 hours), while the Philippines had the highest standard deviation (304.5 hours). The mean standard deviation was found to be 87.4 hours.

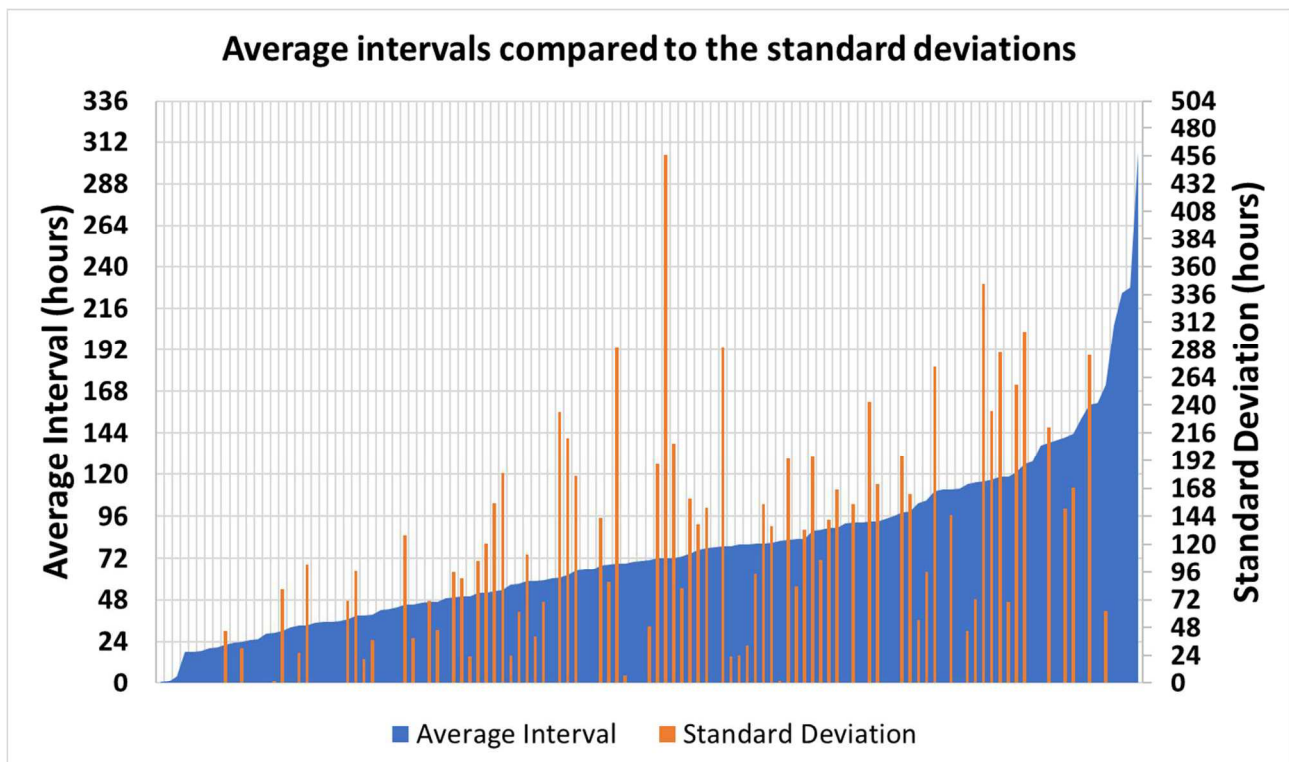


**Fig. 12 – Standard deviation of average intervals.** In the graph above, the average intervals and the standard deviations were compared. The average intervals of the countries analyzed (121 countries) are shown in blue, ordered from left to right with a progressively higher average interval. Credits: G. Cataldi, D. Cataldi, V. Straser.

The standard deviation of Japan (1.5 hours) and China (4.5 hours) are very interesting: these two countries are the ones that have less variability in the correlated time intervals between increases in solar ion flux and M6+ seismic activity. Italy, for example, has a standard deviation of 58.3 hours; Russia 100.7 hours; Greece 192.9 hours; Philippines 304.5 hours. Furthermore, the graph showed two standard deviation peaks: the first peak concerns the countries that have obtained an average interval between 70 and 120 hours; while the second peak concerns the countries that achieved an average interval between 138 and 210 hours. Below are the complete data of the average intervals (in hours) and standard deviations (in hours) of the 121 countries considered in the study:

| Country                    | Average interval (hours) | Standard deviation (hours) |
|----------------------------|--------------------------|----------------------------|
| Albania                    | 0.4                      |                            |
| Yemen                      | 1                        |                            |
| Carlsberg Ridge            | 6                        |                            |
| Bonin Islands              | 27                       |                            |
| Central Mid-Atlantic Ridge | 27new                    |                            |
| Jamaica                    | 28                       |                            |
| South Indian Ocean         | 30                       |                            |
| Cayman Islands             | 31                       |                            |
| Bristol Island             | 33.5                     | 30.1                       |
| Malaysia                   | 35                       |                            |
| Oregon                     | 36                       | 20                         |
| Nevada                     | 37                       |                            |
| Hawaii                     | 38                       |                            |

|                                |        |       |
|--------------------------------|--------|-------|
| Franz Josef Land               | 43     |       |
| Shetland Islands               | 43.5   | 0.7   |
| Indian Ocean                   | 45.25  | 54    |
| Iceland                        | 48     |       |
| Visokoi Island                 | 49.5   | 17.6  |
| Barbados                       | 49.5   | 68.5  |
| Australia                      | 52     |       |
| North Atlantic Ocean           | 53     |       |
| Southwest of Africa            | 53     |       |
| North Indian Ocean             | 54     |       |
| Venezuela                      | 55.5   | 47.3  |
| Thailand                       | 58.5   | 64.3  |
| Nepal                          | 58.5   | 14.1  |
| Ecuador                        | 59.1   | 24.8  |
| Honduras                       | 63     |       |
| Myanmar                        | 64     |       |
| Kyrgyzstan                     | 65     |       |
| Turkey                         | 67.6   | 85.4  |
| Panama                         | 67.8   | 26    |
| Mid-Indian Ridge               | 69     |       |
| Canada                         | 70     | 47.4  |
| Afghanistan                    | 70.4   | 30.3  |
| Marocco                        | 73     |       |
| Pacific-Antarctic Ridge        | 74.16  | 63.7  |
| Drake Passage                  | 74.5   | 60.1  |
| Tajikistan                     | 75     | 15.5  |
| New Caledonia                  | 77.5   | 70.8  |
| Western Indian-Antarctic Ridge | 78     | 80.5  |
| Argentina                      | 79.5   | 103.7 |
| Balleny Islands                | 80.2   | 120.8 |
| Northern Mid-Atlantic Ridge    | 85.1   | 16.1  |
| Kazakhstan                     | 86     | 41    |
| Iran                           | 88     | 74.4  |
| Banda Sea                      | 88     | 26.8  |
| New Zealand                    | 88.5   | 46.5  |
| Southeast Indian Ridge         | 90     |       |
| California                     | 91.5   | 156   |
| Mariana Islands                | 93.6   | 141.1 |
| Chile                          | 97.7   | 119.3 |
| Barbuda                        | 98     |       |
| Chermabura Island              | 98     |       |
| Indonesia                      | 102.2  | 95.2  |
| Italy                          | 103    | 58.3  |
| Fiji Islands                   | 103.5  | 193.2 |
| China                          | 103.8  | 4.5   |
| India                          | 105    |       |
| Indian Ridge                   | 106    |       |
| East Pacific Rise              | 107    | 32.7  |
| Puerto Rico                    | 108    | 125.8 |
| Philippines                    | 108.1  | 304.5 |
| Papua New Guinea               | 108.7  | 137.8 |
| Mexico                         | 110.11 | 54.7  |
| Colombia                       | 112.6  | 106   |
| East Timor                     | 115.5  | 91.6  |
| Russia                         | 116.6  | 100.7 |
| Southern Mid-Atlantic Ridge    | 118    |       |



|                            |       |       |
|----------------------------|-------|-------|
| Greece                     | 118.1 | 192.9 |
| Alaska                     | 118.7 | 15.3  |
| Tonga                      | 120.4 | 16.2  |
| Micronesia                 | 120.4 | 21.9  |
| Izu Island                 | 121   | 63    |
| Ascension Island           | 121.2 | 102.8 |
| El Salvador                | 121.6 | 90.2  |
| Japan                      | 122.8 | 1.5   |
| Solomon Islands            | 123.6 | 128.8 |
| Costa Rica                 | 124.5 | 55.3  |
| Prince Edward Islands      | 124.5 | 88.6  |
| Jan Mayen Island           | 132   | 130.1 |
| Wallis and Futuna          | 132.6 | 71    |
| Sandwich Islands           | 133.8 | 93.9  |
| Bolivia                    | 134.5 | 111.2 |
| Falkland Islands Region    | 138   |       |
| Macquarie Island           | 138.6 | 102.7 |
| South Atlantic Ocean       | 139   |       |
| Peru                       | 139.2 | 162   |
| Burma                      | 139.3 | 114.5 |
| Idaho                      | 142   |       |
| Mindanao                   | 144   |       |
| Amsterdam Island           | 147.5 | 130.8 |
| Guatemala                  | 148   | 108.6 |
| Taiwan                     | 155   | 36.1  |
| Kuril Islands              | 157.3 | 63.7  |
| Easter Island Region       | 165   | 182.1 |
| Indian-Antarctic Ridge     | 167   |       |
| Pakistan                   | 167.3 | 96.8  |
| Scott Island Bank          | 168   |       |
| Vanuatu                    | 172   | 30    |
| Brazil                     | 172.8 | 48.4  |
| Southern East Pacific Rise | 173.7 | 230   |
| Kermadec Islands           | 175.5 | 156.6 |
| Sumatra                    | 178   | 190.5 |
| Molucca Sea                | 178   | 46.6  |
| Central East Pacific Rise  | 181.5 | 171.8 |
| Mauritius                  | 189   | 202.2 |
| Norwegian Sea              | 191   |       |
| Owen Fracture Zone Region  | 205   |       |
| Nicaragua                  | 207.8 | 147   |
| Iraq                       | 210   |       |
| Northern East Pacific Rise | 212   | 100.4 |
| Bouvet Island              | 215.3 | 112.3 |
| Mid Atlantic Ridge         | 229   |       |
| Santa Cruz Islands         | 240.5 | 188.8 |
| Loyalty Islands            | 242   |       |
| Scotia Sea                 | 257.6 | 41.4  |
| Kepulauan Mentawai Region  | 309   |       |
| Botswana                   | 337   |       |
| Christmas Island           | 342   |       |
| Guam                       | 460   |       |

If we analyze the distribution of the countries with respect to the average intervals (**Fig. 13**), we discover that most of these (39.7%) have average intervals between 96 and 168 hours (4-7 days); in second place we find the group of countries (28.1%) which, on the other hand, has average intervals between 48 and 96 hours (2-4

days). Both of these groups make up 67.8% of the countries. It is therefore evident that only 2.5% of the countries in which a potentially destructive seismic event was recorded between 2012 and 15 July 2020, the average time differences recorded between the increases in solar ion flux and the earthquakes related to them lasted a maximum of 24 hours.

### Distribution of countries with respect to average intervals

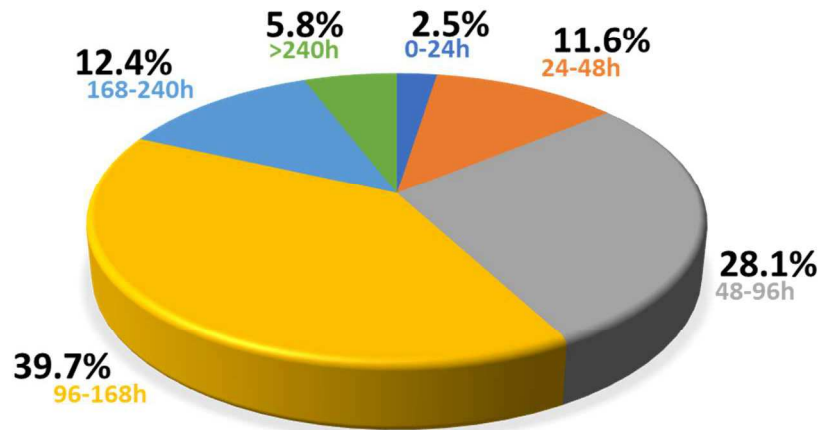


**Fig. 13 – Distribution of countries with respect to average intervals.** The distribution of countries with respect to average intervals is visible in the top graph. The country distribution was divided into 6 groups: 0-24h (within 1 day), 24-48h (between 1 and 2 days), 48-96h (between 2 and 4 days), 96-168h (between 4 and 7 days), 168-240h (between 7 and 10 days) and > 240h (over 10 days). Credits: G. Cataldi, D. Cataldi, V. Straser.

Below are the names of the countries divided by groups with respect to average intervals, as specified in **Fig. 13**:

- Potentially destructive seismic events occurred within 24 hours (1 day) from the beginning of the increase in the density of the solar ion flux (3 countries out of 121; 2.5%): Albania, Yemen, Carlsberg Ridge;
- Potentially destructive seismic events occurred within 24-48 hours (1-2 days) from the beginning of the increase in the density of the solar ion flux (14 out of 121 countries; 11.6%): Bonin Islands, Central Mid-Atlantic Ridge, Jamaica, South Indian Ocean, Cayman Islands, Bristol Island, Malaysia, Oregon, Nevada, Hawaii, Franz Josef Land, Shetland Islands, Indian Ocean, Iceland;
- Potentially destructive seismic events occurred within 48-96 hours (2-4 days) from the beginning of the increase in the density of the solar ion flux (34 countries out of 121; 28.1%): Visokoi Island, Barbados, Australia, North Atlantic Ocean, Southwest of Africa, North Indian Ocean, Venezuela, Thailand, Nepal, Ecuador, Honduras, Myanmar, Kyrgyzstan, Turkey, Panama, Mid-Indian Ridge, Canada, Afghanistan, Morocco, Pacific-Antarctic Ridge, Drake Passage, Tajikistan, New Caledonia, Western Indian-Antarctic Ridge, Argentina, Balleny Islands, Northern Mid-Atlantic Ridge, Kazakhstan, Iran, Banda Sea, New Zealand, Southeast Indian Ridge, California, Mariana Islands;
- Potentially destructive seismic events occurred within 96-168 hours (4-7 days) from the beginning of the increase in the density of the solar ion flux (48 countries out of 121; 39.7%): Chile, Barbuda, Chermabura Island, Indonesia, Italy, Fiji Islands, China, India, Indian Ridge, East Pacific Rise, Puerto Rico, Philippines, Papua New Guinea, Mexico, Colombia, East Timor, Russia, Southern Mid-Atlantic Ridge, Greece, Alaska, Tonga, Micronesia, Izu Island, Ascension Island, El Salvador, Japan, Solomon Islands, Costa Rica, Prince Edward Islands, Jan Mayen Island, Wallis and Futuna, Sandwich Islands, Bolivia, Falkland Islands Region, Macquarie Island, South Atlantic Ocean, Peru, Burma, Idaho, Mindanao, Amsterdam Island, Guatemala, Taiwan, Kuril Islands, Easter Island Region, Indian-Antarctic Ridge, Pakistan, Scott Island Bank;

- Potentially destructive seismic events occurred within 168-240 hours (7-10 days) from the beginning of the increase in the density of the solar ion flux (15 out of 121 countries; 12.4%): Vanuatu, Brazil, Southern East Pacific Rise, Kermadec Islands, Sumatra, Molucca Sea, Central East Pacific Rise, Mauritius, Norwegian Sea, Owen Fracture Zone Region, Nicaragua, Iraq, Northern East Pacific Rise, Bouvet Island, Mid Atlantic Ridge;
- Potentially destructive seismic events that occurred over 240 hours (over 10 days) from the beginning of the increase in the density of the solar ion flux (7 countries out of 121; 5.8%): Santa Cruz Islands, Loyalty Islands, Scotia Sea, Kepulauan Mentawai Region, Botswana, Christmas Island, Guam.

## Discussion

During the twentieth century, for many decades, scientists from around the world have tried to find a possible candidate precursor of potentially destructive earthquakes that occur on a global scale. Although many scientists have noticed a close correlation between solar activity and M6+ global seismic activity, in fact, no one has ever been able to definitively identify the existence of a physical phenomenon related to M6+ global seismic activity that could allow making seismic forecasts on a global scale. This milestone was reached only in 2012 (G. Cataldi et al., 2013) thanks to the work of the authors who first noticed a 100% correlation between the variations of the solar ion flux (proton density) and the M6+ global seismic activity. To date (15 July 2020), the number of potentially destructive seismic events related to a single proton increase in the solar wind is equal to 2.91; while the average interval measured between the beginning of the proton increase (beginning of the Interplanetary Seismic Precursor) and the related seismic event, is equal to 4.76 days (**Fig. 14**). This data has a great predictive significance since if the seismic forecasting method developed by the authors were used on a global scale to understand when to expect a resumption of potentially destructive seismic activity, we would know that the average warning would be equal to 4.76 days: a time interval that can certainly allow all countries located in geographic regions with a high seismic risk to prepare.

Another proof of the impact that solar activity has on M6+ global seismic activity derives from the number of seismic events recorded annually on Earth: the authors established that this follows the trend of the solar cycle, as presented in **Fig. 2** (chapter “Methods and data”). Furthermore, analyzing the data on the daily number of sunspots to the daily number of M6+ seismic events that occurred on a global scale in the period from 2012 to 2018, it emerged that the two phenomena are significantly correlated: when the number of sunspots is at a minimum, the number of seismic events decreases or tends to decrease; while when the daily number of sunspots increases, we observe a higher number of seismic events per day or a higher frequency of single seismic events that occur over the period (days) in which we observe the increase in solar activity. This type of correlation seems to have a connection with the studies conducted by the authors over the last ten years (G. Cataldi et al., 2019).

Since the variations in the density of the solar wind related to the M6+ seismic activity vary as a function of the electromagnetic activity visible in the solar atmosphere (sunspots, coronal holes, solar coronal mass ejections, solar flares), the authors were able to identify three types of Seismic Electromagnetic Precursors (SEPs) each of which precedes the next and can be easily identified:

1. Solar Seismic Precursors (SSPs);
2. Interplanetary Seismic Precursors (ISPs);
3. Seismic Geomagnetic Precursors (SGPs) or Electromagnetic Seismic Precursors (SEPs) of “non-local” type.

These three types of Seismic Electromagnetic Precursors have the characteristic of manifesting themselves in a very precise order (**Fig. 15**): analyzing backward the physical mechanisms responsible for the variation of the proton density of the solar wind, it is clear that the first type of seismic precursors related to M6+ global seismic activity is represented by the electromagnetic activity visible in the solar atmosphere (sunspots, coronal holes, coronal mass ejections, solar flares). This type of electromagnetic phenomena represents the electromagnetic substrate responsible of the solar wind density variations that were defined by the authors as “Solar Seismic Precursor (SSPs)”. After leaving the solar atmosphere, the coronal mass ejections propagate within the interplanetary space in the direction of the planets and here we can identify those that run in the direction of the Earth and that sooner or later will interact with the Earth’s magnetosphere: these electronics clouds have been defined by the authors as “Interplanetary Seismic Precursors” (ISPs) and will take on average

2-4 days to reach the Earth in relation to their speed of escape from the Sun (the speed of coronal mass ejection varies from 50 to 2000km/s). The density of these clouds not only varies according to the amount of coronal mass emitted but also varies with respect to the angular width they possess, measured from the center of the Sun ( $10^{\circ}$ - $90^{\circ}$ ). The last type of seismic precursors related to the solar activity that has been identified by the authors is represented by electromagnetic phenomena arising from the electromagnetic interaction that occurs between the solar wind and the Earth's magnetosphere; i.e. the perturbations of the Earth's geomagnetic field: the authors have called these natural radio emissions "Seismic Geomagnetic Precursors" (SGPs) or "Electromagnetic Seismic Precursors" (SEPs) of "non-local" type, and are observed within about 36 hours of the arrival of the solar ion flux (dense) in the Lagrange point L1 (in this point the orbit of the artificial satellite which has the purpose of analyzing the physical characteristics of the solar wind).

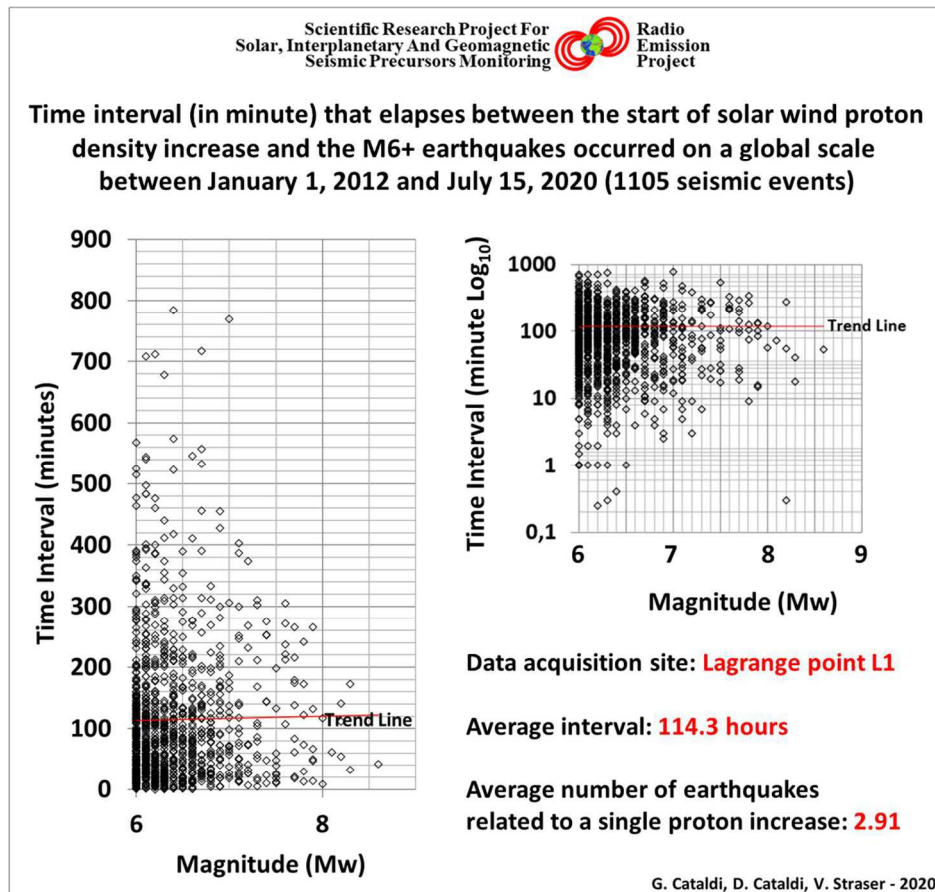


**Fig. 14 – Time interval (in minute) that elapses between the start of solar wind proton density increase and the M6+ earthquakes occurred on a global scale between January 1, 2012 and July 15, 2020.** In the graphs above it is possible to observe the time intervals recorded between the increases in the proton density of the solar wind and the M6+ global seismic activity that occurred between January 1, 2012 and July 15, 2020: a sample of 1105 seismic events analyzed by the authors at starting from 2012. Credits: Gabriele Cataldi, Daniele Cataldi, Valentino Straser.

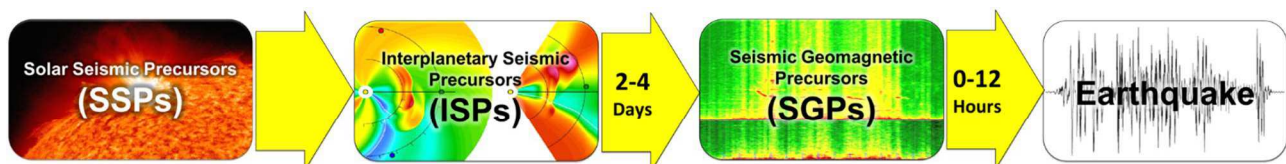


**Fig. 15 – Types of Electromagnetic Seismic Precursors (ESPs) identified in 2012 by the authors.** The representation above shows the temporal order of Electromagnetic Seismic Precursors (ESPs) identified by the authors during 2012 and presented to the international scientific community in 2013 (G. Cataldi et al., 2013). Credits: Gabriele Cataldi, Daniele Cataldi, Valentino Straser.

As for the seismogenic mechanism that would be the basis of the close correlation that the authors have identified between the variation in the density of the solar ion flux and the M6+ seismic activity that occurs on

a global scale, it is evident that this must be a form of electromagnetic interaction: the variations of the solar ion flux that interact with the terrestrial magnetosphere produce a series of perturbations of the terrestrial geomagnetic field that can produce deformations of the crystal grid of the rocks included in the fault planes by inverse piezoelectric effect and through magnetostriction. The deformation of the rocks can therefore alter the static balance of the faults producing earthquakes (V. Straser et al., 2020). In fact, the study carried out by the authors showed that the higher the level of proton density, the greater the number of seismic events related to it, and the greater the magnitude. In fact, it has been noted several times that large increases in the proton density of the solar wind are followed by a greater number of M6+ seismic events than more modest increases. This could, in fact, be explained by the production of a more intense and lasting geomagnetic perturbation which is capable of generating a greater and more lasting deformation of the crystal grid of the rocks included in the fault planes. The magnitude of M6+ seismic events also appears to be related to the extent of the variation in the density of the solar ion flux: seismic events with high magnitude (M7+) are generally correlated to increases in the solar ion flux that reach higher levels than those related to seismic events with lower magnitude, and this can always depend on the extent of the geomagnetic perturbation induced (greater) by high increases in the solar ion flux and by the inverse piezoelectric and magnetostrictive effect that follows.

Between 2019 and July 26, 2020, for example, the M7+ seismic events were mainly correlated to increases in the proton density of the solar wind that reached a density of at least  $20\text{p}/\text{cm}^3$  but if we observe the value of the proton density measured precisely at the time the earthquake was recorded, the M7+ seismic winds occurred in the same time frame are correlated to an average proton density of  $5\text{p}/\text{cm}^3$ . Recall that the average density of M6+ seismic events recorded between 2019 and July 26, 2020, is equivalent to  $5.6\text{p}/\text{cm}^3$  with a standard deviation of  $6.61\text{p}/\text{cm}^3$ .

Another aspect that is important to underline concerns the energetic fraction of the solar ion flux that is used to perform a correlation study with these characteristics: the type of measurement that is carried out on the ion flux can give different results. For example, considering proton values expressed in  $\text{p}/\text{cm}^3$  with respect to  $\text{p}/(\text{cm}^2\text{-sec-ster-MeV})$ , slightly lower time intervals are obtained. Furthermore, by analyzing the curves of the proton fractions of the solar wind it was established that:

- there is a progressive decrease in the magnitude of M6+ seismic trains that occurred after a determined proton increase in the solar wind (G. Cataldi et al., 2013-2017; G. Cataldi et al., 2019; G. Cataldi, 2020; D. Cataldi et al., 2014; D. Cataldi et al., 2017; T. Rabeh et al., 2014; V. Straser, 2011-2012; V. Straser et al., 2014-2017; V. Straser, 2017; V. Straser et al., 2019);
- protons with higher energies vary more abruptly than protons that have lower energy fractions: this can cause slightly different results on time differences if energy fractions of a certain type are used rather than others. Different results are also obtained when analyzing the time intervals taking as a reference the maximum deviation of the proton density rather than the density value recorded at the time the earthquake occurred. Understandably, the question is not simple.

The authors coined an acronym to define the level of proton density beyond which an earthquake is produced: “Electromagnetic Seismic Trigger Threshold” (ESTT). This level, for the reasons we have just described, is very variable, and even if for the M7+ seismic events a minimum value of proton density equivalent to  $20\text{p}/\text{cm}^3$  has been mainly identified, at the present state of knowledge it is not possible to identify a precise proton density level beyond which a seismic event is triggered that has a minimum magnitude of 6 because observations have shown that global seismic activity with magnitude M6+ can be triggered even with proton density values just above the basal level (**Fig. 16**). The threshold, in fact, must be identified by analyzing the curve of variation of the proton density of the solar wind, also in relation to the SEPs (Solar Energetic Particles) events already in progress; and this is because it is not always possible to obtain proton density readings stabilized on basal values. However, what the authors clarified is that the ESTT always respects the distribution indicated in **Fig. 1** (chapter “Methods and data”).

Understanding the exact value of the ESTT of a given M6+ seismic event is not easy: if on the one hand, the authors have understood that every M6+ seismic event that occurs on a global scale is preceded by an increase in the proton density of the solar wind, It is also true that there is the practical difficulty of determining which is the exact point of the variation curve that must be taken as a reference to establish when an M6+ seismic event will occur in a certain way. To obtain this result, the authors verified the value of the proton density of



the solar wind at the time when the M6+ seismic events occurred on a global scale between January 1, 2019 and July 26, 2020. (**Fig. 16**).

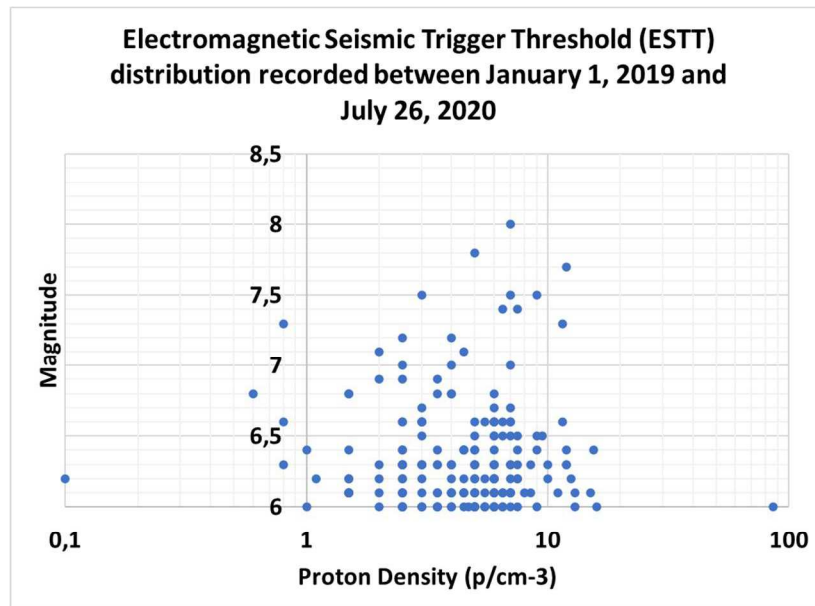


**Fig. 16 – Electromagnetic Seismic Trigger Threshold (ESTT) distribution.** The graph above shows the Electromagnetic Seismic Trigger Threshold (ESTT) distribution recorded between January 1, 2019 and July 26, 2020. Credits: Gabriele Cataldi, Daniele Cataldi, Valentino Straser.

In **Fig. 17** the ESTT average was calculated based on magnitude. Also, in this case, the data on M6+ seismic activity and solar activity was acquired between January 1, 2019, and July 26, 2020.

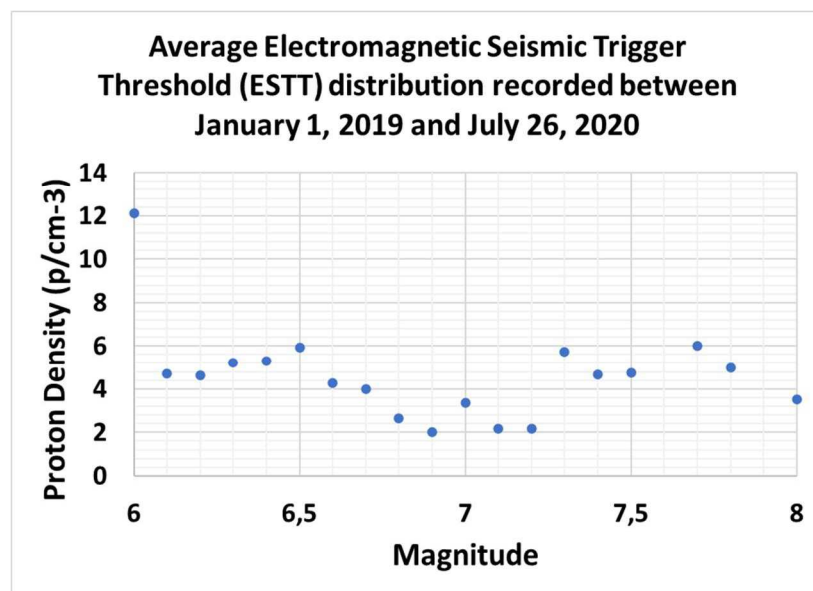


**Fig. 17 – Average Electromagnetic Seismic Trigger Threshold (ESTT) distribution.** The graph above shows the average Electromagnetic Seismic Trigger Threshold (ESTT) distribution recorded between January 1, 2019 and July 26, 2020. Credits: Gabriele Cataldi, Daniele Cataldi, Valentino Straser.

Observing **Fig. 17** it is possible to understand that the average Electromagnetic Seismic Trigger Threshold (ESTT) associated with earthquakes of magnitude 6 is very high, but this happened due to a seismic event that reached an ESTT of 85.9 p/cm<sup>3</sup>: this increased the average ESTT for earthquakes of magnitude 6. As regards the average ESTT of the other magnitudes, it is evident that this is placed between 2 and 6 p/cm<sup>3</sup>, albeit with a certain variability.

This result does not allow us to have a precise indication of the magnitude of an M6+ seismic event by interpreting the values of the proton density of the solar wind without evaluating the variation curve; in fact, from a predictive point of view, the studies conducted by the authors since 2012 on the proton variation curve of the solar wind have shown that it is more convenient to focus attention on:

- the point (temporal marker) of the beginning of the proton increase (beginning of Interplanetary Seismic Precursor) for the seismic events that occur during the phase of the proton increase (phase A, **Fig. 1; Fig. 18**) and the maximum phase density reached (phase B, **Fig. 1; Fig. 18**);
- the maximum value of the proton density reached for the seismic events that occur during the phase of reduction of the proton density (phase C and D, **Fig. 1; Fig. 18**).

The identification of the starting point of the proton increase is fundamental as the variation curve can be identified as an Interplanetary Seismic Precursor (ISP). By following this evaluation method it was possible to correlate all M6+ seismic events occurring on a global scale to increases in the proton density variation. Furthermore, this method allows you to make a forecast on a global scale of the period in which it is possible to expect a resumption of M6+ seismic activity.

### Structural anatomy of an Interplanetary Seismic Precursor (solar wind proton density increase related to the M6+ global seismic activity)

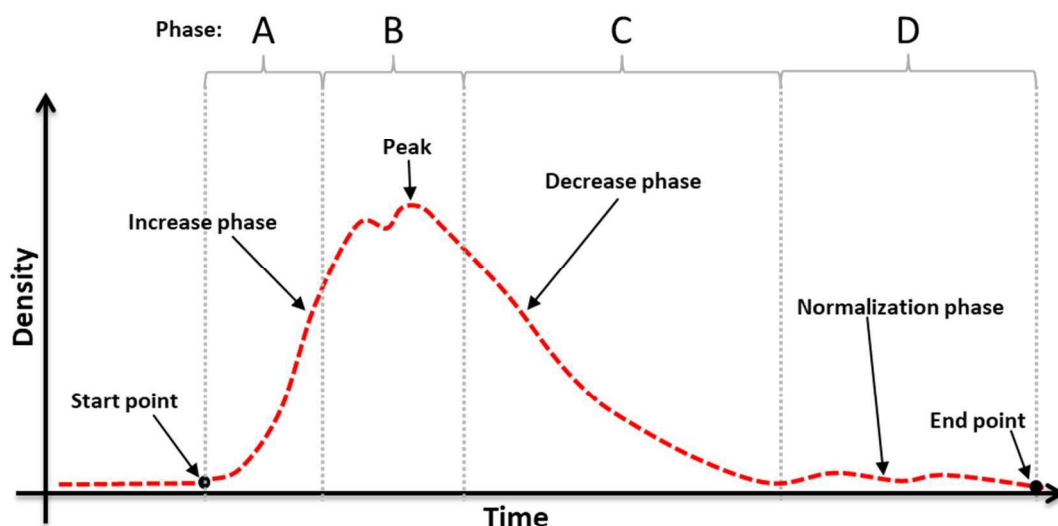


**Fig. 18 – Structural anatomy of an Interplanetary Seismic Precursor.** In the representation above, the structural anatomy of an Interplanetary Seismic Precursor is visible. The dashed red line represents the variation curve of the proton density measured at the Lagrangian point L1 by artificial satellites. Credits: Gabriele Cataldi, Daniele Cataldi, Valentino Straser.

As has already been repeated in the first chapter, 49.58% of the potentially destructive earthquakes that are recorded on a global scale occur after the maximum peak reached by the proton density of the solar wind, that is during the phase of reduction of the proton density (phase C); 31.87% of destructive seismic events occur during the increase in proton density (phase A), while the remaining 18.55 of potentially destructive seismic events occur during the maximum peak reached by proton density (phase B) and during the normalization phase (phase D). According to the data, it is evident that most of the potentially destructive seismic events (81.45%; phase A + phase C) occur during a variation of the proton density and not during what can be defined as a “leveling” of the same. According to the authors, the reason can be traced back to the relapse that has a sudden change in the density of the solar ion flux on the Earth’s geomagnetic field: sudden fluctuations in the proton density produce more intense geomagnetic perturbations and, these, more intensely stress the crystalline grid of the rocks included in the fault plane through the inverse piezoelectric effect and through magnetostriction; phenomena which, according to the authors, would be at the basis of the seismogenesis related to the variation of the proton density. But that is not all.

Laboratory experiments conducted on a few cubic centimeters of rock have found that during the creation of fractures in rocks, as a result of mechanical stress, emitted a significant amount of radio waves through the

phenomenon of piezoelectricity. This phenomenon is observed when crystals are applied to some of the mechanical stress in certain crystallographic directions: the opposite sides of the crystals we load instantly (Finkelstein et al., 1973). Studies confirming the production of radiofrequency emitted by rocks placed under mechanical stress have also been conducted in recent years thanks to the funds allocated by NASA (National Aeronautics and Space Administration) (F. Freund, 2002). When tectonic stress accumulates along a fault, the crystal grid of some rocks can emit pre-seismic radiofrequency (V. Straser et al., 2020; G. Cataldi, 2020); this electromagnetic emission source can be detected by radio receivers tuned in the SELF-LF band ( $>0.96000$  Hz). If you have a network of electromagnetic monitoring stations equipped with “Radio Direction Finder” (RDF) technology, through the triangulation method it is possible to identify the geographical areas from which these radio emissions are emitted, allowing us to understand where the epicenter of an imminent earthquake is located. Since 2019, the authors have developed a technology capable of performing a multi-parametric crustal diagnosis remotely through:

- the “Radio Direction Finder” (RDF) technology applied to the pre-seismic radio frequency scanning in the SELF-LF band (0-96kHz);
- the detection of the concentration of the Radon<sub>222</sub> gas flow.

This technique made it possible to identify some epicentral Italian and international areas with an average notice of 20 hours. The data obtained through this type of innovative approach towards local and global seismicity have been presented to the international scientific community starting from 2018 (V. Straser et al., 2018-2020; D. Cataldi et al., 2019-2020; F. Di Stefano et al., 2020).

## Conclusions

The short-term and long-term analysis of the solar ion flux characteristics allowed the authors to ascertain that the changes in the proton density of the interplanetary medium that occurred between January 1, 2012, and July 15, 2020, always precede potentially destructive seismic events (M6+) with an average time interval of 114.3 hours (4.76 days) (G. Cataldi et al., 2013-2017; G. Cataldi et al., 2019; G. Cataldi, 2020; D. Cataldi et al., 2014; D. Cataldi et al., 2017; T. Rabeh et al., 2014; V. Straser, 2011-2012; V. Straser et al., 2014-2017; V. Straser, 2017; V. Straser et al., 2019). This result is obtainable only by considering the entire proton variation curve as a seismic precursor (more precisely: an “Interplanetary Seismic Precursor”). The distribution of potentially destructive seismic events (M6+) that were recorded on a global scale with respect to the proton variation curve allowed to highlight that 81.45% of earthquakes occur during a variation of the proton density (increase or decrease), while 18.55% occurs during a horizontalization phase of the variation curve. The authors believe that M6+ global seismic activity and solar activity are correlated through a form of electromagnetic interaction identifiable through variations or perturbations of the Earth’s geomagnetic field (Seismic Geomagnetic Precursors or Seismic Electromagnetic Precursors of “non-local” type) which determine an elastic deformation of the crystalline grid present in the rocks included in the fault plane of the seismically active areas through the phenomenon of inverse piezoelectricity and magnetostriction phenomena, which together with the tectonic stress provided by geodynamics also contribute to the production of pre-seismic electromagnetic dipoles in the focal area of the earthquake through the variation of volumes and spaces that separate the constituent elements of the Earth’s crust (rocks). Through a network of multi-parametric monitoring stations equipped with broadband radio receivers implemented with Radio Direction Finder (RDF) technology and sensors for monitoring the Radon<sub>222</sub> gas flow, it is possible to obtain indications on the geographical position of this source of pre-seismic electromagnetic emission (V. Straser et al., 2018-2020; D. Cataldi et al., 2019-2020; F. Di Stefano et al., 2020) which, due to its characteristics, the authors called “Seismic Electromagnetic Precursors “Local” type (SEPs).

The authors believe it is convenient to use this new global seismic forecasting method as an indicator capable of defining when to expect a resumption of seismic activity on a global scale.

## Bibliography

- D. Cataldi, G. Cataldi, and V. Straser. (2014). Variations of the Electromagnetic field that preceded the Peruvian M7.0 earthquake occurred on September 25, 2013. European Geosciences Union (EGU) General Assembly 2014, Geophysical Research Abstract, Vol. 16, Natural Hazard Section (NH4.3), Electro-magnetic phenomena and connections with seismo-tectonic activity, Vienna, Austria.

Harvard-Smithsonian Center for Astrophysics, High Energy Astrophysics Division, SAO/NASA Astrophysics Data System.

- D. Cataldi, G. Cataldi, V. Straser. (2017). SELF and VLF electromagnetic emissions that preceded the M6.2 Central Italy earthquake occurred on August 24, 2016. European Geosciences Union (EGU), General Assembly 2017. Seismology (SM1.2)/Natural Hazards (NH4.7)/Tectonics & Structural Geology (TS5.5) The 2016 Central Italy Seismic sequence: overview of data analyses and source models. Geophysical Research Abstracts Vol. 19, EGU2017-3675, 2017. Harvard-Smithsonian Center for Astrophysics, High Energy Astrophysics Division, SAO/NASA Astrophysics Data System.
- D. Cataldi, G. Cataldi, V. Straser. (2019). Radio Direction Finding (RDF) - Pre-seismic signals recorded before the earthquake in central Italy on 1/1/2019 west of Collelongo (AQ). European Geosciences Union (EGU) General Assembly 2019, Seismology (SM1.1) General Contributions on Earthquakes, Earth Structure, Seismology, Geophysical Research Abstract, Vol. 21, EGU2019-3124, 2019, Vienna, Austria. Harvard-Smithsonian Center for Astrophysics, High Energy Astrophysics Division, SAO/NASA Astrophysics Data System.
- D. Cataldi, G. G. Giuliani, V. Straser, G. Cataldi. (2020). Radio signals and changes of flow of Radon gas (Rn222) which led the seismic sequence and the earthquake of magnitude Mw 4.4 that has been recorded in central Italy (Balsorano, L'Aquila) on November 7, 2019. An international journal for New Concepts in Geoplasma Tectonics, Volume 8, Number 1, May 2020, pp. 32-42.
- D. Finkelstein, U. S. Hill, J. R. Powell. (1973). The piezoelectric theory of earthquake lightning. J. Geophys. Res., 78, 992-993.
- D. V. Reames, Astrophysical J. 571, L63 (2002).
- F. Di Stefano, G. Giuliani, D. Ouzounov, D. Cataldi, C. Fidani, A. D'Errico, G. Fioravanti. (2020). Support for preventions and preparedness of the strait of Messina. Reggio Calabria – An earthquake forecasting project. Atti della Accademia Peloritana dei Pericolanti Classe di Scienze Fisiche, Matematiche e Naturali. May 4, 2020.
- F. Freund. (2002). Charge generation and propagation in igneous rocks. Special Issue of the Journal of Geodynamics. NASA Ames Research Center; Moffett Field, CA United States.
- G. Cataldi, D. Cataldi, V. Straser. (2013). Variations Of Terrestrial Geomagnetic Activity Correlated To M6+ Global Seismic Activity. EGU (European Geosciences Union) 2013, General Assembly, Seismology Section (SM3.1), Earthquake precursors, bio-anomalies prior to earthquakes and prediction, Geophysical Research Abstracts, Vol. 15. Vienna, Austria. Harvard-Smithsonian Center for Astrophysics, High Energy Astrophysics Division, SAO/NASA Astrophysics Data System.
- G. Cataldi, D. Cataldi and V. Straser. (2014). Earth's magnetic field anomalies that precede the M6+ global seismic activity. European Geosciences Union (EGU) General Assembly 2014, Geophysical Research Abstract, Vol. 16, Vienna, Austria. Natural Hazard Section (NH4.3), Electro-magnetic phenomena and connections with seismo-tectonic activity, Harvard-Smithsonian Center for Astrophysics, High Energy Astrophysics Division, SAO/NASA Astrophysics Data System.
- G. Cataldi, D. Cataldi, V. Straser. (2015). Solar wind proton density variations that preceded the M6+ earthquakes occurring on a global scale between 17 and 20 April 2014. European Geosciences Union (EGU) General Assembly 2015, Vienna, Austria. Natural Hazard Section (NH5.1), Sea & Ocean Hazard - Tsunami, Geophysical Research Abstract, Vol. 17, Harvard-Smithsonian Center for Astrophysics, High Energy Astrophysics Division, SAO/NASA Astrophysics Data System.

- G. Cataldi, D. Cataldi, V. Straser. (2015). Solar wind ion density variations that preceded the M6+ earthquakes occurring on a global scale between 3 and 15 September 2013. European Geosciences Union (EGU) General Assembly 2015, Geophysical Research Abstract, Vol. 17, Vienna, Austria. Natural Hazard Section (NH5.1), Sea & Ocean Hazard - Tsunami, Harvard-Smithsonian Center for Astrophysics, High Energy Astrophysics Division, SAO/NASA Astrophysics Data System.
- G. Cataldi, D. Cataldi, V. Straser. (2015). Solar wind proton density variations that preceded the M6,1 earthquake occurred in New Caledonia on November 10, 2014. European Geosciences Union (EGU) General Assembly 2015, Geophysical Research Abstract, Vol. 17, Vienna, Austria. Natural Hazard Section (NH5.1), Sea & Ocean Hazard - Tsunami, Harvard-Smithsonian Center for Astrophysics, High Energy Astrophysics Division, SAO/NASA Astrophysics Data System.
- G. Cataldi, D. Cataldi, V. Straser. (2016). Solar activity correlated to the M7.0 Japan earthquake occurred on April 15, 2016. New Concepts in Global Tectonics Journal, V. 4, No. 2, June 2016.
- G. Cataldi, D. Cataldi, V. Straser. (2016). Tsunami related to solar and geomagnetic activity. European Geosciences Union (EGU) General Assembly 2016, Natural Hazard Section (NH5.6), Complex modeling of earthquake, landslide, and volcano tsunami sources. Geophysical Research Abstract, Vol. 18, Vienna, Austria. Harvard-Smithsonian Center for Astrophysics, High Energy Astrophysics Division, SAO/NASA Astrophysics Data System.
- G. Cataldi, D. Cataldi, V. Straser. (2017). SELF-VLF electromagnetic signals and solar wind proton density variations that preceded the M6.2 Central Italy earthquake on August 24, 2016. International Journal of Modern Research in Electrical and Electronic Engineering, Vol. 1, No. 1, 1-15, 2017. DOI: 10.20448/journal.526/2017.1.1/526.1.1.15. Harvard-Smithsonian Center for Astrophysics, High Energy Astrophysics Division, SAO/NASA Astrophysics Data System.
- G. Cataldi, D. Cataldi, V. Straser. (2017). Solar and Geomagnetic Activity Variations Correlated to Italian M6+ Earthquakes Occurred in 2016. European Geosciences Union (EGU), General Assembly 2017. Geophysical Research Abstracts Vol. 19, EGU2017-3681, 2017. Seismology (SM1.2)/Natural Hazards (NH4.7)/Tectonics & Structural Geology (TS5.5) The 2016 Central Italy Seismic sequence: overview of data analyses and source models. Harvard-Smithsonian Center for Astrophysics, High Energy Astrophysics Division, SAO/NASA Astrophysics Data System.
- G. Cataldi, D. Cataldi, V. Straser. (2017). Solar wind proton density increase that preceded Central Italy earthquakes occurred between 26 and 30 October 2016. European Geosciences Union (EGU), General Assembly 2017. Geophysical Research Abstracts Vol. 19, EGU2017-3774, 2017. Seismology (SM1.2)/Natural Hazards (NH4.7)/Tectonics & Structural Geology (TS5.5) The 2016 Central Italy Seismic sequence: overview of data analyses and source models. Harvard-Smithsonian Center for Astrophysics, High Energy Astrophysics Division, SAO/NASA Astrophysics Data System.
- G. Cataldi, D. Cataldi, V. Straser. (2019). Solar wind ionic density variations related to M6+ global seismic activity between 2012 and 2018. European Geosciences Union (EGU) General Assembly 2019, Short-term Earthquake Forecast (StEF) and multy-parametric time-Dependent Assessment of Seismic Hazard (t-DASH) (NH4.3/AS4.62/EMRP2.40/ESSI1.7/Gi2.13/SM3.9), General Contribution on Earthquakes, Earth Structure, Seismology (SM1.1), Geophysical Research Abstract, Vol. 21, EGU2019-3067, 2019, Vienna, Austria. Harvard-Smithsonian Center for Astrophysics, High Energy Astrophysics Division, SAO/NASA Astrophysics Data System.
- G. Cataldi, D. Cataldi, V. Straser. (2019). Wolf Number Related To M6+ Global Seismic Activity. New Concepts in Global Tectonics Journal, Volume 7, Number 3, December 2019, pp. 179-186.
- G. Cataldi. (2020). Precursori Sismici – Monitoraggio Elettromagnetico. Kindle-Amazon, ISBN: 9798664537970. ASIN Code: B08CPDBGX9.



- J. A. Broun. (1861). On the horizontal force of the Earth's magnetism, Proc. Roy. Soc. Edinburgh, 22, 511.
- K. Ohta, J. Izutsu, A. Schekotov, and M. Hayakawa (2013), The ULF/ELF electromagnetic radiation before the 11 March 2011 Japanese earthquake, Radio Sci., 48, 589–596, doi:10.1002/rds.20064.
- N. A. F. Moos. (1910). Magnetic observations made at the government observatory, Bombay, for the period 1846 to 1905, and their discussion, Part II: the phenomenon and its discussion, Bombay.
- T. Rabeh, G. Cataldi, V. Straser. (2014). Possibility of coupling the magnetosphere–ionosphere during the time of earthquakes. European Geosciences Union (EGU) General Assembly 2014, Geophysical Research Abstract, Vol. 16, Vienna, Austria. Natural Hazard Section (NH4.3), Electro-magnetic phenomena and connections with seismo-tectonic activity. Harvard-Smithsonian Center for Astrophysics, High Energy Astrophysics Division, SAO/NASA Astrophysics Data System.
- V. Straser. (2011). Radio Wave Anomalies, Ulf Geomagnetic Changes And Variations In The Interplanetary Magnetic Field Preceding The Japanese M9.0 Earthquake. New Concepts in Global Tectonics Newsletter, no. 59, June, 2011. Terenzo PR, Italy.
- V. Straser. (2011). Radio Anomalies And Variations In The Interplanetary Magnetic Field Used As Seismic Precursor On A Global Scale, New Concepts in Global Tectonics Newsletter, no. 61, December, 2011. Terenzo PR, Italy.
- V. Straser. (2012). Can IMF And The Electromagnetic Coupling Between The Sun And The Earth Cause Potentially Destructive Earthquakes? New Concepts in Global Tectonics Newsletter, no. 65, December, 2012. Terenzo PR, Italy. Society for Interdisciplinary Studies (SIS).
- V. Straser. (2012). Intervals Of Pulsation Of Diminishing Periods And Radio Anomalies Found Before The Occurrence of M6+ Earthquakes. New Concept in Global Tectonics Newsletter, no. 65, December, 2012. Terenzo PR, Italy.
- V. Straser, G. Cataldi. (2014). Solar wind proton density increase and geomagnetic background anomalies before strong M6+ earthquakes. Space Research Institute of Moscow, Russian Academy of Sciences, MSS-14. 2014. Moscow, Russia.
- V. Straser, G. Cataldi. (2015). Solar wind ionic variation associated with earthquakes greater than magnitude M6.0. New Concepts in Global Tectonics Journal, V. 3, No. 2, June 2015, Australia. P.140-154.
- V. Straser, G. Cataldi, D. Cataldi. (2015). Solar wind ionic and geomagnetic variations preceding the Md8.3 Chile Earthquake. New Concepts in Global Tectonics Journal, V. 3, No. 3, September 2015, Australia. P.394-399.
- V. Straser, G. Cataldi, D. Cataldi. (2016). SELF and VLF electromagnetic signal variations that preceded the Central Italy earthquake on August 24, 2016. New Concepts in Global Tectonics Journal, V. 4, No. 3, September 2016. P.473-477. Harvard-Smithsonian Center for Astrophysics, High Energy Astrophysics Division, SAO/NASA Astrophysics Data System.
- V. Straser, G. Cataldi, D. Cataldi. (2017). Solar and electromagnetic signal before Mexican Earthquake M8.1, September 2017. New Concepts in Global Tectonics Journal, V. 5, No. 4, December 2017.
- V. Straser. (2017). Plasmas in the atmosphere, tectonics and earthquake: a possible link for the crustal diagnosis? American Geophysical Union, Fall Meeting 2017, abstract #NH21C-0178.

- V. Straser, D. Cataldi, G. Cataldi. (2018). Radio Direction Finding System, a new perspective for global crust diagnosis. *New Concepts in Global Tectonics Journal*, V. 6, No. 2, June 2018.
- V. Straser, H. Wu, A. Bapat, N. Venkatanathan, Z. Shou, G. Gregori, B. Leybourne, L. Hissink. (2019) Multi-parametric Earthquake Forecasting From Electromagnetic Coupling between Solar Corona and Earth System Precursors. 21st EGU General Assembly, EGU2019, Proceedings from the conference held 7-12 April, 2019 in Vienna, Austria, id.5976. Harvard-Smithsonian Center for Astrophysics, High Energy Astrophysics Division, SAO/NASA Astrophysics Data System.
- V. Straser, D. Cataldi, G. Cataldi. (2019). Registration of Pre-Seismic Signals Related to the Mediterranean Area with the Rdf System Developed by the Radio Emissions Project. *International Journal of Engineering Science Invention (IJESI)*, www.ijesi.org. Volume 8 Issue 03 Series. March 2019. PP 26-35. ISSN (Online): 2319 – 6734, ISSN (Print): 2319 – 6726. 2019.
- V. Straser, D. Cataldi, G. Cataldi. (2019). Radio Direction Finding (RDF) - Geomagnetic Monitoring Study of the Himalaya Area in Search of Pre-Seismic Electromagnetic Signals. *Asian Review of Environmental and Earth Sciences*, v. 6, n. 1, p. 16-27, 14 jun. 2019
- V. Straser, D. Cataldi, G. Cataldi. (2019). Electromagnetic monitoring of the New Madrid fault us area with the RDF system - Radio Direction Finding of the radio emissions project. *New Concepts in Global Tectonics Journal*, V7 N1, March 2019.
- V. Straser, G. Cataldi, D. Cataldi. (2019). Namazu's Tail – RDF: a new perspective for the study of seismic precursors of Japan. *Lulu Editore*, 2019.
- V. Straser, G. G. Giuliani, D. Cataldi, G. Cataldi. (2020). Multi-parametric investigation of pre-seismic origin phenomena through the use of RDF technology (Radio Direction Finding) and the monitoring of Radon gas stream (RN222). *An international journal for New Concepts in Geoplasma Tectonics*, Volume 8, Number 1, May 2020, pp. 11-27.
- W. G. Adams. (1982). Comparison of simultaneous magnetic disturbance at several observatories, *Phil. Trans. London (A)*, 183, 131.